

# Can the anisotropic hydraulic conductivity of an aquifer be determined using surface displacement data? A case study

Sona Salehian Ghamsari <sup>a</sup>,\* , Tonie van Dam <sup>b</sup>, Jack S. Hale <sup>a</sup>

<sup>a</sup> Institute of Computational Engineering, Department of Engineering, Faculty of Science, Technology, and Medicine, University of Luxembourg, 6 avenue de la Fonte, Esch-sur-Alzette, L-4364, Luxembourg

<sup>b</sup> Department of Geology and Geophysics, College of Mines and Earth Sciences, University of Utah, 201 Presidents' Cir, Salt Lake City, 84112-0102, UT, United States

## ARTICLE INFO

Dataset link: [Supplementary material for "Can the anisotropic hydraulic conductivity of an aquifer be determined using surface displacement data? A case study"](#)

### Keywords:

Anisotropic hydraulic conductivity  
Poroelasticity  
Aquifer systems  
InSAR  
Finite element method

## ABSTRACT

Due to geological features such as fractures, some aquifers demonstrate strongly anisotropic hydraulic behavior. The goal of this study is to use a poroelastic model to calculate surface displacements given known pumping rates to predict the potential utility of Interferometric Synthetic Aperture Radar (InSAR) data for inferring information about anisotropic hydraulic conductivity (AHC) in aquifer systems. To this end, we develop a three-dimensional anisotropic poroelastic model mimicking the main features of the 1994 Anderson Junction aquifer test in southwestern Utah with a 24 to 1 ratio of hydraulic conductivity along the principal axes, previously estimated in the literature using traditional well observation techniques. Under suitable model assumptions, our results show that anisotropy in the hydraulic problem leads to a distinctive elliptical surface displacement pattern centered around the pumping well that could be detected with InSAR. We interpret these results in the context of InSAR acquisition constraints and provide guidelines for designing future pumping tests so that InSAR data can be used to its full potential for improving the characterization of aquifers with anisotropic hydraulic behavior.

## 1. Introduction

Groundwater is a vital resource that provides drinking water to billions of people and supports critical agriculture and industrial activities (Food and Agriculture Organization of the United Nations (FAO), 2022). One of the biggest challenges for sustainability of global groundwater resources is overexploitation (Basu and Van Meter, 2014; Caretta et al., 2022). The consequences of overexploitation include reducing the amount of water available to surface water bodies (Walker et al., 2020), lowering the water table to the extent that it leads to surface subsidence (Heilweil and Hsieh, 2006; Burbey et al., 2006; Galloway and Burbey, 2011) and saltwater intrusion (Guo et al., 2019b). Overexploitation of groundwater resources is a global issue with the largest impacts in areas with high population densities, rapid urbanization and agricultural intensification (Poland, 1984; Famiglietti et al., 2011; Erkens et al., 2015).

Consequently, there is a need for increased research and monitoring to understand better the complex hydrological processes that govern groundwater systems and contribute data to support effective management strategies. To this end, groundwater modeling and simulation tools have become an increasingly important component in supporting

decision-makers to design effective strategies (Singh, 2014; Amitrano et al., 2014). One aspect of ensuring that groundwater simulation tools can produce reasonable predictions is ensuring that all possible data sources are assimilated into the model for e.g. parameter inference. Specifically, in this study, we ask “is there potentially valuable information in Interferometric Synthetic Aperture Radar (InSAR) data for inferring anisotropic hydraulic conductivity (AHC) in a poroelastic model of an aquifer?”. This question forms part of broader research efforts on developing new approaches for assimilating remote sensing data into hydrogeomechanical models of aquifers – however, we do not tackle the data assimilation problem here.

The use of InSAR in hydrogeological research has become increasingly popular due to its high precision in measuring ground surface displacement, wide-area coverage and cost-effectiveness (Guzy and Malinowska, 2020; Galloway and Hoffmann, 2007). InSAR observations of surface uplift and subsidence allow inference of groundwater levels and flow gradients (Gambolati and Teatini, 2015). InSAR observations can be used to determine the structural boundaries of aquifer systems (Chaussard et al., 2014; Haghighi and Motagh, 2019; Hu and Bürgmann, 2020), provide the temporal evolution of the ground

\* Corresponding author.

E-mail addresses: [salehiyan.sona@gmail.com](mailto:salehiyan.sona@gmail.com) (S. Salehian Ghamsari), [tonie.vandam@utah.edu](mailto:tonie.vandam@utah.edu) (T. van Dam), [mail@jackhale.co.uk](mailto:mail@jackhale.co.uk) (J.S. Hale).

surface (Zhou et al., 2018; Guo et al., 2019a; Boniet al., 2017) and to contribute to estimate storage coefficients and hydraulic conductivity (Hu et al., 2018; Boniet al., 2016; Chaussard et al., 2014). Development of InSAR technology has contributed to the regional hydrogeological models of groundwater flow and land deformation (Galloway and Hoffmann, 2007; Gambolati and Teatini, 2015). Since the accuracy of the InSAR measurement is the most important parameter for the estimation of the aquifer properties (Guzy and Malinowska, 2020) and using InSAR time-series enhances the accuracy of surface displacement estimation (Li et al., 2022), consequently using InSAR time-series would improve the accuracy of estimating aquifer properties.

The pumping of subsurface fluids during an aquifer test causes a drop in pore pressure which leads to a three-dimensional deformation. This response has been simulated using a number of modeling approaches, see e.g. Guzy and Malinowska (2020). While conventional groundwater flow theory in the aquitard drainage model has been widely used (Helm, 1986; Harbaugh et al., 2000; Hoffmann et al., 2003; Harbaugh, 2005) it has been argued that the use of numerical poroelasticity models is necessary for realistic aquifer settings (Hsieh, 1996). The theory of poroelasticity introduced by Biot (1941) describes the interactions between water, the porous matrix of rock and solid grains. This theory explains how changes in pressure and fluid content within the porous matrix can cause deformation and stress among the solid grains, and vice versa. Verruijt (1969) proposed a formulation of Biot's linear theory that is suitable for problems in soil mechanics. In the context of calibrating groundwater flow models with InSAR-derived displacement data, it is necessary to use a model that directly links fluid flow to deformation by including poroelasticity theory.

The underlying cause of AHC in hydrogeology is often a preferential rock fracturing direction that allows for higher fluid conductivity along the direction of fractures (Berre et al., 2019). The recognition of the importance of AHC on the behavior of aquifer systems dates back to the work of Papadopoulos (1965) who presented a method to determine the hydraulic conductivity of a homogeneous anisotropic aquifer from the observation of pressure (head drop) at a minimum of three wells situated at different directions around a constant-rate aquifer extraction test. Heilweil and Hsieh (2006) demonstrated that AHC could be inferred from two observation wells, if the wells are assumed to be aligned with the principal directions of AHC. The possibility was also mentioned by Burbey (2006).

In the specific context of AHC and geodesy, both Burbey et al. (2006) and Burbey (2006) proposed that the elliptical vertical surface displacement pattern observed from Global Positioning System (GPS) receivers positioned around a Nevada pumping test could be directly related to the interaction between an anisotropy in the fluid flow and rock skeleton. In support of this theory, Burbey (2006) presented computer simulations based on a poroelasticity theory showing elliptical vertical displacement patterns at the Earth's surface under a 3 to 1 AHC ratio. The elliptical pattern in the displacements is driven by the underlying anisotropy in the fluid problem caused by the fractures tendency to provide directional conduits for flow.

Galloway and Hoffmann (2007) showed that InSAR can be used to calibrate numerical models of groundwater flow and deformation. Galloway and Burbey (2011) conducted a review of various remote sensing techniques and models used for studying subsidence due to groundwater extraction. Hesse and Stadler (2014) proposed scalable computational methods for assimilating InSAR data into a poroelastic finite element model with spatially varying isotropic hydraulic conductivity within a Bayesian framework. Continuing with the line of work developed by Hesse and Stadler (2014), recently (Alghamdi, 2020; Alghamdi et al., 2020, 2021) assimilated InSAR data from the test site of Burbey et al. (2006) into a spatially-varying isotropic hydraulic conductivity (IHC) poroelastic model. We remark that in the original study of Burbey et al. (2006) it is mentioned that due to the underlying geology (fracturing) the hydraulic behavior of the site is likely to be strongly anisotropic and therefore the isotropic model used in Alghamdi

(2020) for calibration using the data from Burbey et al. (2006) may be insufficient to fully capture the anisotropic behavior of the site. In addition, the elliptical shape observed in the surface displacement measured by the InSAR technique, as shown in Alghamdi et al. (2020, Figure 1c), may be evidence of anisotropy, as discussed by Burbey (2006).

In this study, we develop a three-dimensional linear poroelastic model that includes AHC to gain insight into the relationship between surface displacement and pumping at Anderson Junction in southwestern Utah. The goal is to use our anisotropic model to calculate surface displacements given known pumping rates to predict the potential utility of InSAR data for inferring information about AHC in aquifer systems. We choose this site because Heilweil and Hsieh (2006) specifically studied the role of anisotropy there, giving estimated AHC ratio of around 24 to 1 determined using two observation wells. Using our model, we predict the InSAR Line of Sight (LOS) displacements for the region, i.e. the quantity of interest for calibration of the model against theoretical InSAR observations (Alghamdi, 2020).

We show that the duration of four days and rate of the pumping used in the Anderson Junction test was likely insufficient to induce surface displacements that can be measured with InSAR. We then run our model under a number of alternative scenarios, including different pumping rates, pumping lengths and anisotropy ratios to determine when the displacements would be observable by InSAR. We conclude that there could be pumping regimes in which InSAR data could contain important information about AHC. Finally, we discuss some guidelines for designing future pumping tests in the context of InSAR acquisition constraints.

An outline of this manuscript is as follows. Section 2 provides an overview of the Anderson Junction study area and the aquifer test. In Section 3, we outline the theoretical foundations by presenting the Biot equations. In Section 4, we introduce the InSAR technique and present the transformation of the three-dimensional deformations into InSAR LOS observations. In Section 5, we describe our proposed model in detail. The outcomes of our simulations are presented in Section 6. Finally, in Section 7 we present the conclusions of our study.

## 2. Case study

Our case study is located at Anderson Junction, Utah, USA, see Fig. 1, and was the subject of the pumping test conducted by the US Geological Survey (USGS) in March and April 1996 to determine the local Navajo Sandstone's anisotropic hydraulic conductivity and storage properties (Heilweil and Hsieh, 2006; Heilweil et al., 2000). The test involved a pumping well (C-40-13)28dcb-2 and two observation wells, well A, (C-40-13)28dca-1 and well B, (C-40-13)28dcc-1 (Survey, 2016). Groundwater was pumped for approximately 4 days at an average rate of  $6000\text{ m}^3\text{ d}^{-1}$ . Pumping then stopped and well observations continued for 20 days.

The site shown in Figs. 2(a) and 2(b) features a confined aquifer characterized by a 180 m thick deposit of Navajo sandstone (Heilweil and Hsieh, 2006). The overlying layer consists of unconsolidated mixed alluvial and colluvial deposits and the underlying layer is the Kayenta formation (Hintze, 1980). The overlying and underlying layers act as confining layers for the aquifer.

The rose diagram Fig. 3(a) shows that the site is strongly characterized by fracturing of the Navajo sandstone, with a primary cluster at  $180^\circ$  to  $210^\circ$ , and a secondary cluster at orientation of  $90^\circ$  to  $130^\circ$ .

The Hurricane Fault and an unnamed series of faults offset the Kayenta Formation and Navajo Sandstone along its length. These faults are assumed to impede groundwater flow perpendicular to their fault planes due to the presence of poorly-sorted breccia and clay-rich materials (Hurlow, 1998).

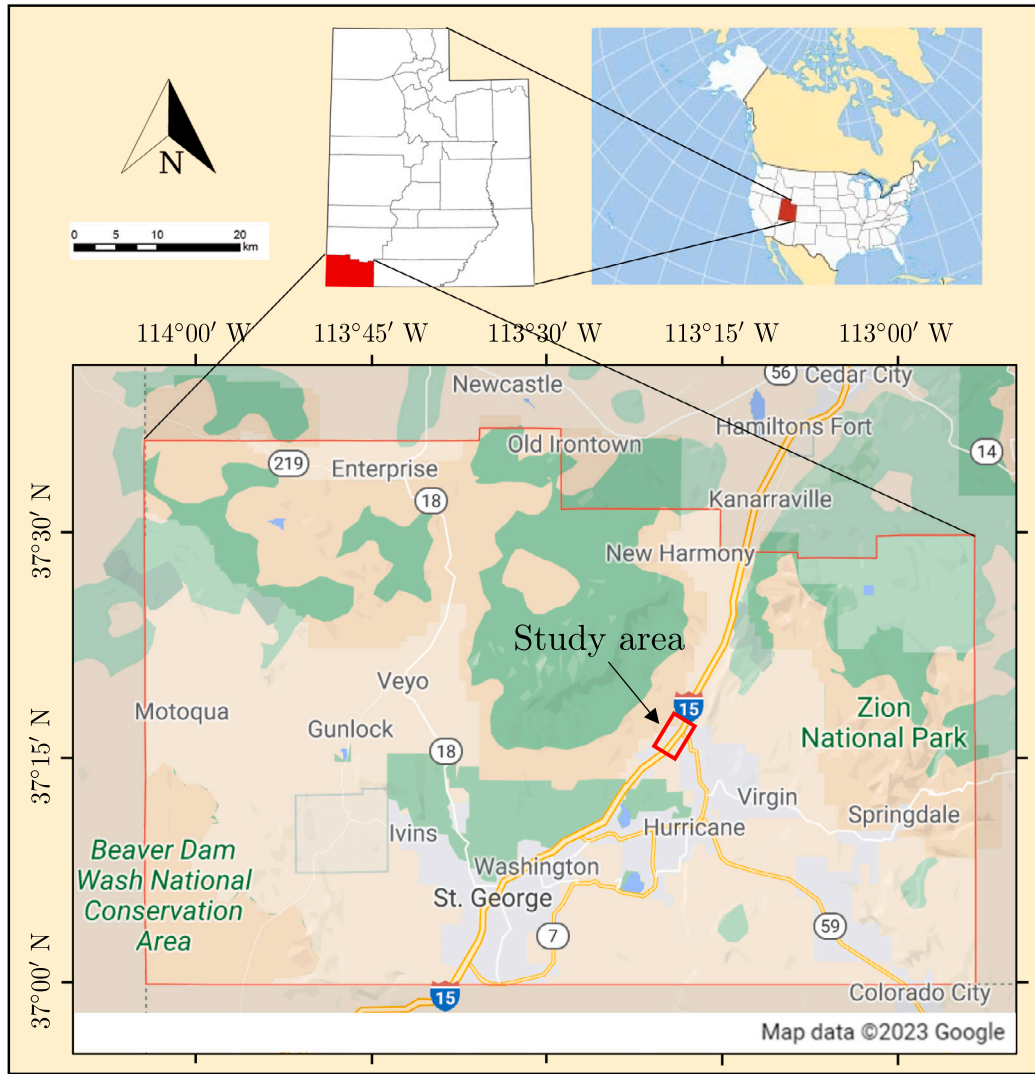


Fig. 1. Location of the Anderson Junction site in Utah, USA. Lower map data Copyright Google 2023. (For interpretation of the references to color in this figure legend, the reader is referred to the web version of this article.)

### 3. Biot's poroelasticity theory

We describe the three-field formulation of Biot's poroelasticity theory following Ferronato et al. (2010) and Alghamdi (2020). This is used to construct the conceptual model of Anderson Junction in Section 5. Full details are given in Appendix A and the code for the solver is included as supplementary material (Salehian Ghamsari and Hale, 2024).

Given a domain  $\Omega \subset \mathbb{R}^3$  with boundary  $\Gamma$  and outward-pointing normal  $n$ , find the fluid-pore pressure  $p : \Omega \times (0, T] \rightarrow \mathbb{R}$ , deformation  $u : \Omega \times (0, T] \rightarrow \mathbb{R}^3$  and fluid flux  $q : \Omega \times (0, T] \rightarrow \mathbb{R}^3$  such that

$$\begin{aligned} (S_\epsilon p + \alpha \nabla \cdot u)_t + \nabla \cdot q &= f_p \text{ on } \Omega \times (0, T], \\ -\nabla \cdot \bar{\sigma}(u, p) &= f_u \text{ on } \Omega \times (0, T], \\ q + k \nabla p &= 0 \text{ on } \Omega \times (0, T], \end{aligned}$$

with notations and units summarized in Table 1, plus boundary conditions

$$\begin{aligned} u &= u_d \text{ on } \Gamma_u^d \times (0, T], \\ \bar{\sigma} \cdot n &= g_u \text{ on } \Gamma_u^n \times (0, T], \\ p &= p_d \text{ on } \Gamma_p^d \times (0, T], \\ q \cdot n &= g_p \text{ on } \Gamma_p^n \times (0, T], \end{aligned}$$

where the boundary  $\Gamma$  has been partitioned into disjoint parts for both the solid problem  $\Gamma = \Gamma_u^d \cup \Gamma_u^n$  and the fluid problem  $\Gamma = \Gamma_p^d \cup \Gamma_p^n$ , plus initial conditions

$$\begin{aligned} p(x, 0) &= p^0 \text{ on } \Omega, \\ u(x, 0) &= u^0 \text{ on } \Omega, \\ q(x, 0) &= q^0 \text{ on } \Omega. \end{aligned}$$

The AHC is modeled as a second-rank symmetric positive definite tensor. When the principal axis of hydraulic conductivity is aligned with the global coordinate system  $(x, y, z)$ , this tensor can be represented as a diagonal matrix with positive entries  $k_{xx}$ ,  $k_{yy}$  and  $k_{zz}$

$$k = \begin{bmatrix} k_{xx} & 0 & 0 \\ 0 & k_{yy} & 0 \\ 0 & 0 & k_{zz} \end{bmatrix}.$$

The elastic stress tensor  $\sigma$  is given for isotropic linear elasticity by Hooke's law

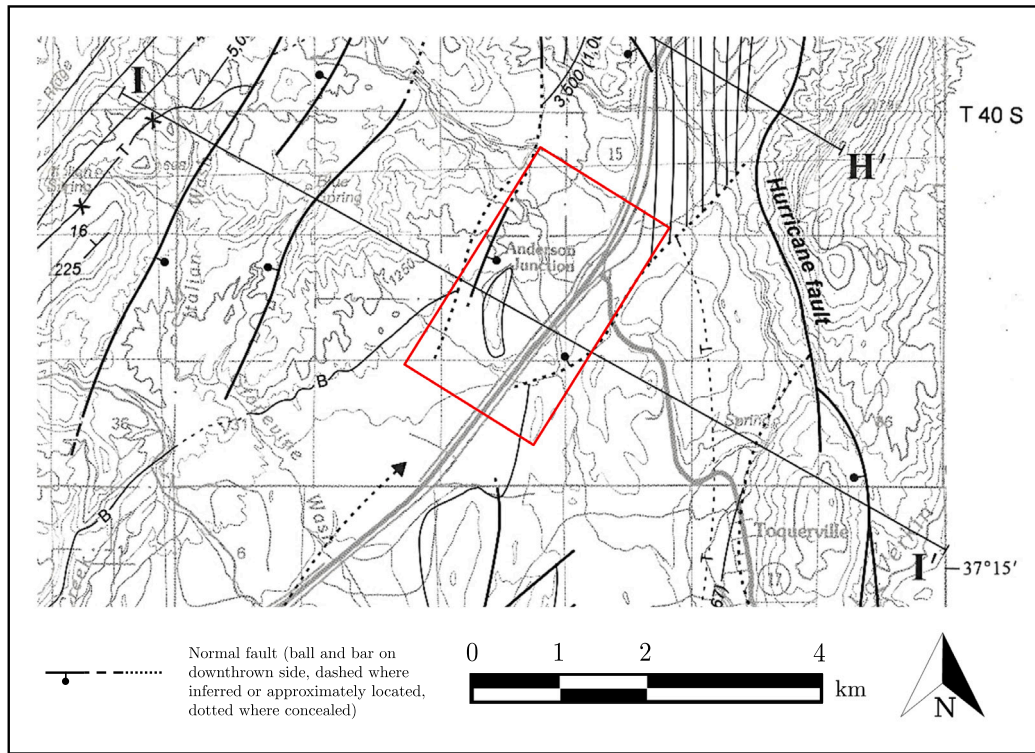
$$\sigma = 2\mu_s \epsilon + \lambda(\text{Tr } \epsilon)I, \quad (1a)$$

$$\epsilon = \frac{1}{2} (\nabla u + (\nabla u)^T), \quad (1b)$$

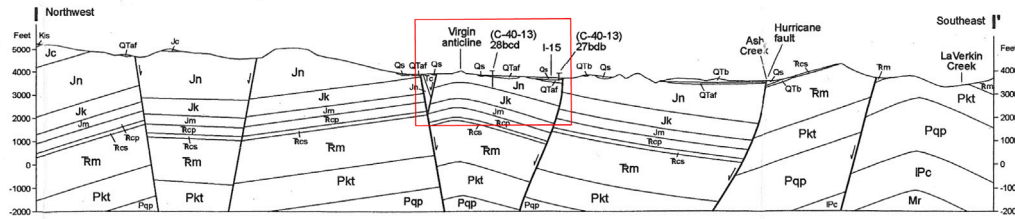
and the Biot stress tensor as

$$\bar{\sigma} = \sigma - \alpha p I, \quad (2)$$





(a) Location of the II' cross-section transect line on structure-contour map.



(b) Geologic cross-section of Anderson Junction site.

**Fig. 2.** Geologic cross-section of Anderson Junction site and its location (Image courtesy of U.S. Geological Survey (Hurflow, 1998) in the U.S. Public Domain.). The study area is highlighted by a red rectangle. The y-axis in the cross-section is elevation in feet with respect to mean sea level. The cross-section reveals the geological layers, including the unconsolidated alluvial and colluvial deposits (Qs) on the surface as the upper confining layer, the Navajo sandstone (Jn) as the aquifer layer, and the Kayenta formation (Jk) as the lower confining layer. In the cross-section, faults are depicted as nearly vertical lines. Note that the orientation of the cross-section aligns with the axis of major hydraulic conductivity shown in Fig. 3(b). (For interpretation of the references to color in this figure legend, the reader is referred to the web version of this article.)

with notations also described in Table 1.

#### 4. Calculation and precision of InSAR-derived displacements

The SAR satellite emits radar pulses in the LOS direction, oriented perpendicular to the satellite's direction of motion, see Fig. 4. Following Fuhrmann and Garthwaite (2019) the displacement in the LOS direction  $u_{LOS}$  can be calculated from the incidence angle  $\theta$  and satellite heading angle  $\alpha$  as

$$u_{LOS} = \begin{bmatrix} -\sin \theta \cos \alpha & \sin \theta \sin \alpha & \cos \theta \end{bmatrix} \begin{bmatrix} u_E \\ u_N \\ u_U \end{bmatrix}. \quad (3)$$

where  $u_E$ ,  $u_N$ , and  $u_U$  are deformation in directions of east, north and up, respectively, that can be calculated by transforming the predicted deformation (Section 3) in the model coordinate system ( $u = (u_x, u_y, u_z)$ ) to east-north-up (ENU) coordinate system as depicted in Fig. 6(a). In our calculations, we use Sentinel-1 ascending geometry values for a NNW ascending satellite pass taking  $\alpha = 15^\circ$  and  $\theta = 43.86^\circ$  (European Space Agency (ESA), 2023).

Several studies have shown that achieving sub-centimeter precision using Sentinel-1 is possible (Cigna et al., 2021). For example, comparisons between Sentinel-1 InSAR data and Global Navigation Satellite System (GNSS) measurements reveal a precision of less than 5 mm (Manunta et al., 2019) or 8 mm (Duan et al., 2020). Consequently, when we analyze the results of the simulations in Section 6, if the computed LOS displacement is greater than 8 mm we will consider the deformation signal detectable.

#### 5. Conceptual model construction

##### 5.1. Aquifer model layers and parameters

The simulated model domain is shown in Fig. 5 with the positions of the pumping and observation wells, along with the  $xx'$  and  $yy'$  lines that will be used later for extracting results for visualization.

The three horizontal layers of the aquifer model are shown in Fig. 6(a). We simplified the geological complexity by assuming horizontal layers for our aquifer model – this assumption is made due to a lack of information about the height of layers throughout the aquifer system.

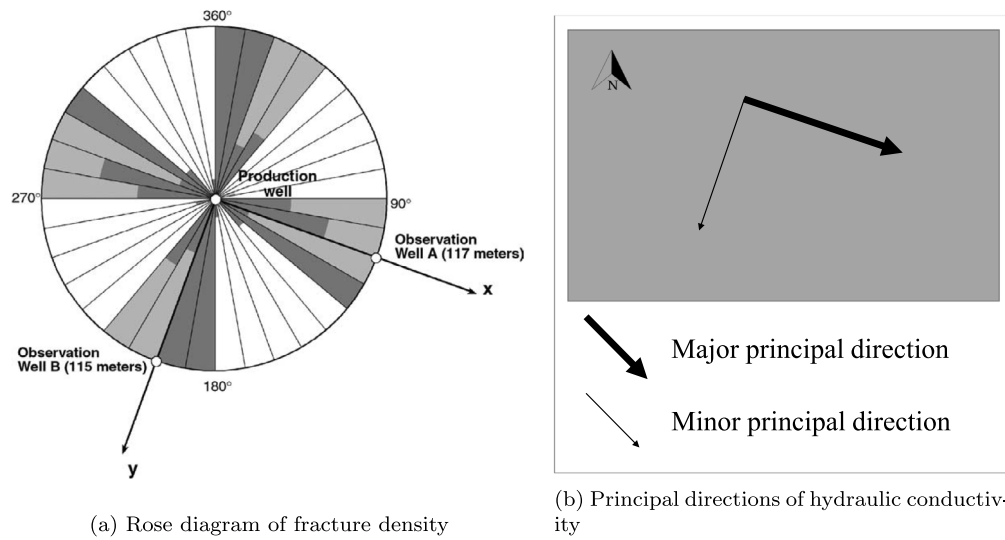


**Fig. 3.** (3(a)). Rose diagram showing fracture orientations (from Heilwell and Hsieh, 2006) and locations of pumping and observation wells used for the Anderson Junction aquifer test. (3(b)). Principal directions of hydraulic conductivity of the Anderson Junction aquifer system were derived from modified Papadopoulos method in Heilwell and Hsieh (2006). Arrows represent major and minor principal directions, indicating that hydraulic conductivity in the major direction is approximately 24 times greater than in the minor direction. Note: Arrow lengths do not signify the scale of hydraulic conductivity.

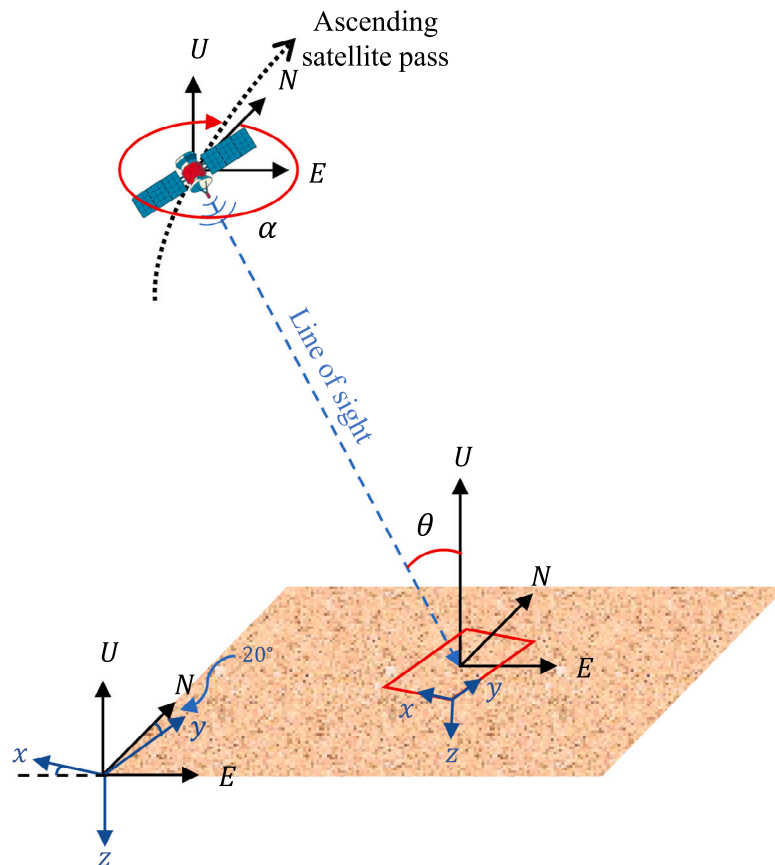


**Fig. 4.** Geometry of SAR Imaging showing the incidence angle ( $\theta$ ) and heading angle ( $\alpha$ ). The study area is highlighted by a red rectangle. (For interpretation of the references to color in this figure legend, the reader is referred to the web version of this article.)

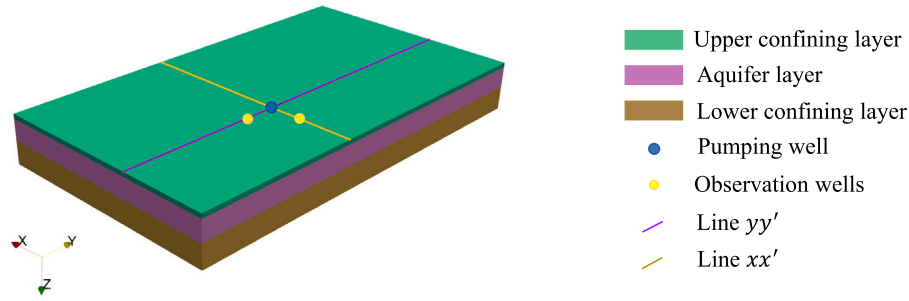


**Fig. 5.** Simulated domain of the aquifer system illustrating the three layers and their element sizes. The figure also highlights the positions of the pumping and observation wells, as well as lines  $xx'$  and  $yy'$ . The  $xx'$  line extends from  $x = 0$  m to  $x = 2000$  m, passing through the pumping well and aligned with the  $X$ -axis, while the  $yy'$  line extends from  $y = 0$  m to  $y = 3500$  m, also passing through the pumping well and aligned with the  $Y$ -axis. (For interpretation of the references to color in this figure legend, the reader is referred to the web version of this article.)

**Table 1**

Table of main notations and units used in the three-field formulation of Biot's poroelasticity theory.

Symbol	Description	Units
$\partial_t$	time derivative	$s^{-1}$
$\nabla$	gradient operator	$m^{-1}$
$\nabla \cdot$	divergence operator	$m^{-1}$
$\text{Tr}$	trace operator	dimensionless
$(\cdot)^T$	transpose operator	dimensionless
$p$	fluid pore pressure	Pa
$u$	elastic deformation	m
$q$	volumetric fluid flux	$m s^{-1}$
$f_p$	fluid source density	$s^{-1}$
$g_p$	boundary fluid flux	$m s^{-1}$
$f_u$	body force density	$N m^{-3}$
$g_u$	traction	Pa
$\sigma$	stress tensor	Pa
$\bar{\sigma}$	Biot stress tensor	Pa
$I$	identity tensor	dimensionless
$\alpha$	Biot coefficient	dimensionless
$S_e$	drained storage coefficient	$Pa^{-1}$
$k$	hydraulic conductivity tensor	$m^3 s kg^{-1}$
$\mu_s$	drained shear modulus	Pa
$\lambda$	second Lamé parameter	Pa

**Table 2**

Model parameters.

Description	Symbol	Unit	Value
Fluid source	$f_p$	$s^{-1}$	0.0
Body force	$f_u$	$N m^{-3}$	0.0
Specific weight of water	$\rho g$	$N m^{-3}$	9807
Pumping rate	$P_r$	$m^3 s^{-1}$	0.07
Pumping area	$A$	$m^2$	1473.4
Pumping time	$T_p$	d	4.0

The aquifer's width and length were estimated based on the map of effective land subsidence due to groundwater depletion (Herrera-García et al., 2021). Table 2 and Table 3 present the model parameters and layer parameters, respectively, that are used in the finite element simulation.

The boundary conditions were established using USGS sources (Marston and Heilweil, 2012; Heilweil et al., 2000) and the parameters of the Biot equations for the aquifer layer were extracted from various regional studies (Torabi et al., 2015; Cheng and Toksöz, 1979; Loope et al., 2020) and sandstone properties studies (Batzle et al., 2007; George et al., 2010; Molina et al., 2017).

The estimate for aquifer hydraulic conductivity was derived from the permeability in Heilweil and Hsieh (2006) following

$$k = \frac{\kappa'}{\rho g}, \quad (4)$$

**Table 3**

Material parameters of the layers. The Anderson Junction site is an extensional tectonic regime, which usually leads to more vertical than horizontal faults, thereby increasing the value of  $k_{zz}$  over  $k_{xx}$  and  $k_{yy}$ .

Description	Symbol	Unit	Upper conf.	Aquifer	Lower conf.
Porosity	$\phi$	—	10%	32%	8%
Biot coefficient	$\alpha$	—	0.868	0.998	0.858
Specific storage	$S_e$	$Pa^{-1}$	$0.8 \times 10^{-10}$	$1.5 \times 10^{-10}$	$0.8 \times 10^{-10}$
Shear modulus	$\mu_s$	Pa	$7.7 \times 10^9$	$5.06 \times 10^9$	$7.9 \times 10^9$
Lame's first param.	$\lambda$	Pa	$6.088 \times 10^9$	$3.768 \times 10^9$	$6.156 \times 10^9$
Hydraulic conductivity $xx$	$k_{xx}$	$m^3 s kg^{-1}$	$5 \times 10^{-12}$	$1.1 \times 10^{-8}$	$5 \times 10^{-12}$
Hydraulic conductivity $yy$	$k_{yy}$	$m^3 s kg^{-1}$	$5 \times 10^{-12}$	$4.7 \times 10^{-10}$	$5 \times 10^{-12}$
Hydraulic conductivity $zz$	$k_{zz}$	$m^3 s kg^{-1}$	$5 \times 10^{-12}$	$5 \times 10^{-7}$	$5 \times 10^{-12}$

**Table 4**

Boundary conditions of fluid and solid problem. The boundary sets are defined in Fig. 6(b).

	Boundary condition	Boundary
Fluid problem ( $q, p$ )	$q \cdot n = 0$	$\Gamma_b \cup \Gamma_{xx} \cup \Gamma_{yy} \cup \Gamma_l \cup \Gamma_w$
	$q \cdot n = g_p = -P_r/A$	$\Gamma_{pw}$
	$u = 0$	$\Gamma_b$
	$u_x = 0$	$\Gamma_{xx}$
Solid problem ( $u$ )	$u_y = 0$	$\Gamma_{yy}$
	$\sigma \cdot n = 0$	$\Gamma_l \cup \Gamma_{pw}$
	$u \cdot n = 0$	$\Gamma_w$

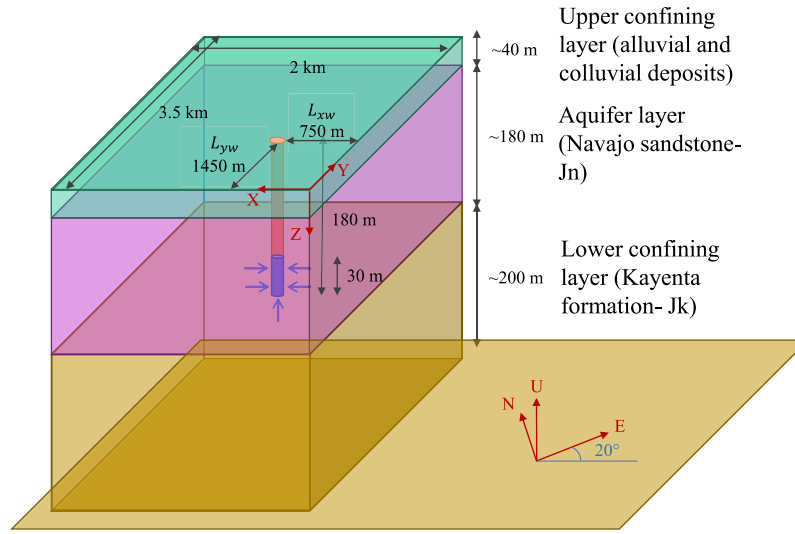
where  $k$  is the hydraulic conductivity,  $\kappa'$  is the specific permeability of the porous medium and  $\rho g$  is the fluid's specific weight.

For the confining layer properties we employ porosity-based estimation (Dehghani et al., 2018). We used Dehghani et al. (2018, Figure 5) for approximating the Biot coefficient, Dehghani et al. (2018, Figure 7) for Biot's modulus, Dehghani et al. (2018, Figure 8b) for Young's modulus and Dehghani et al. (2018, Figure 9) for the shear modulus. We suppose the porosity of the upper confining layer to be 10% following the suggestion of 7% to 10% in Qi et al. (2022) and Earle (2019). Considering the general trend of decreasing porosity and permeability with depth below the land surface (Herod, 2013), we assume the porosity of the lower confining layer to be 8%. The average total porosity of the aquifer layer was derived from Heilweil et al. (2000).

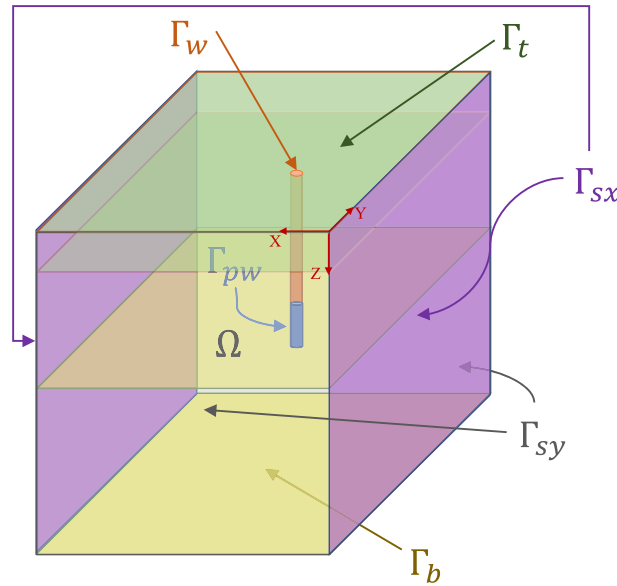
## 5.2. Boundary conditions

Table 4 shows the boundary conditions for the state variables  $u$  (displacement),  $p$  (pressure) and  $q$  (flux). The boundaries referenced in the table are defined in Fig. 6(b).

During the aquifer test period, precipitation and evapotranspiration is assumed to be negligible compared with pumping, allowing us to assume no recharge through the top boundary  $\Gamma_t$ . We also assume no fluid flux on all other boundaries due to the presence of faults,



(a) Simplified conceptual model of the Anderson Junction aquifer system.



(b) Aquifer model illustrating the domain and defined boundaries.

**Fig. 6.** (6(a)). Simplified conceptual model of the Anderson Junction aquifer system showcasing the dimensions, names, formations, and thicknesses of the layers within the cross-section. The pumping well is accurately positioned and labeled in the 3D model. The figure also illustrates the model coordinate system in relation to the ENU global coordinate system. (6(b)). Aquifer model illustrating the domain and defined boundaries referenced in Table 4, domain not to scale.  $\Gamma_b$  is the bottom boundary,  $\Gamma_t$  is the top boundary,  $\Gamma_{sx}$  is the two sides with normal facing in the  $X$ -direction,  $\Gamma_{sy}$  is two sides with normal facing in the  $Y$ -direction,  $\Gamma_w$  is the well boundary from the surface until the end of the casing set and  $\Gamma_{pw}$  is the screened area of the well boundary where water is pumped. Both domains are not to scale. (For interpretation of the references to color in this figure legend, the reader is referred to the web version of this article.)

except the pumping well boundary  $\Gamma_{pw}$ , where the extraction rate  $g_p$  is specified.

As the study area is not urban, the top boundary  $\Gamma_t$  is considered traction-free. We also assume there is no displacement on the bottom boundary  $\Gamma_b$ . We also assume zero normal displacement at the side boundaries  $\Gamma_{sx}$  and  $\Gamma_{sy}$  and well boundary  $\Gamma_w$ , and traction-free boundary conditions at the top surface  $\Gamma_t$  and at the pumping well boundary  $\Gamma_{pw}$ .

### 5.3. Main modeling assumptions

We briefly discuss the main modeling assumptions and their justification. Our modeling approach is a parsimonious one, prioritizing model simplicity over capturing all possible features of the real Anderson Junction site.

As in Burbey (2006), we assume a purely elastic deformation of the skeleton, i.e. no inelastic deformation. This is an acceptable assumption in the context of a single constant pumping cycle (as opposed to cyclic and/or pulsed pumping), however, this elasticity assumption may be invalid if we wanted to simulate subsidence across multiple seasons and using more complex pumping regimes.

We assume that seasonal recharge and evapotranspiration is zero; for this site this is a valid assumption if the pumping test occurs during the summer months due to the cold semi-arid (steppe) climate (BSk - Köppen type system).

The solid boundary condition on the capped well boundary  $\Gamma_{pw}$  is zero normal component of the deformation. The physicality of this boundary condition is discussed in Burbey (2006); in summary, it is likely that deformation near the well boundary are inaccurate due to

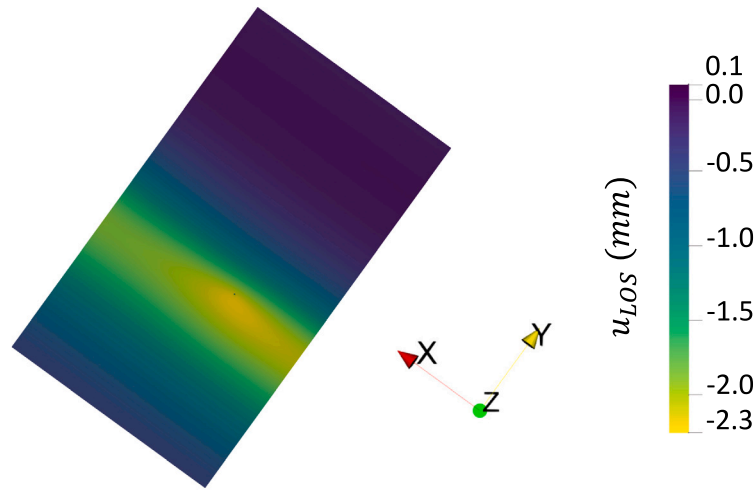


Fig. 7. Simulated LOS surface displacement at the end of pumping for Anderson Junction test (4d,  $P_r$ ).

localized effects such as sand grains near the well screen not being radially constrained during strong pumping. Consequently, the deformation and flux patterns given by the simulation in the region immediately around the well should be considered as indicative or approximate, rather than precise.

We do not model the fluid flow through fractures in our model explicitly, e.g. Berre et al. (2019), but instead incorporate their dominating effect on the fluid flow through the anisotropic hydraulic conductivity tensor. In the broader context of data assimilation, it is unlikely that SAR or GPS displacement data could be sufficiently informative to constrain information about microstructural features such as individual fracture paths. Further on this point of information content, we remark that Alghamdi (2020) demonstrated that SAR data is not informative about the variability of hydraulic conductivity in the vertical ( $z$ ) direction. With this limited information content in mind, we also assume that the global anisotropic behavior of the model is in the fluid problem, i.e. we treat the solid problem as isotropic. This is the same assumption used in Burbey (2006).

## 6. Results and discussion

### 6.1. Simulation of the Anderson Junction pumping test

Fig. 7 shows the simulated LOS displacement after four days of pumping. The areas close to the pumping well exhibit LOS displacements on the order of 2.3 mm. The larger vertical displacements along the  $x$  direction (versus the  $y$  direction) are driven by the higher hydraulic conductivity in the  $x$  direction.

### 6.2. The effect of anisotropy ratio on the surface displacement

We now conduct simulations with varying anisotropy ratios. Fig. 8 presents the surface displacement for three simulated scenarios at three times through the pumping phase. The scenarios are IHC with  $k_{xx} = k_{yy} = 0.6 \times k_{yy}^{AJ}$ ; AHC with a 3:1 anisotropy ratio, similar to the anisotropy observed in Burbey et al. (2006), Burbey (2006), where  $k_{xx} = 3 \times 1.7 \times k_{yy}^{AJ}$  and  $k_{yy} = 1.7 \times k_{yy}^{AJ}$ ; and AHC with an anisotropy ratio of about 24:1, representative of the Anderson Junction aquifer, where  $k_{xx}^{AJ}$  and  $k_{yy}^{AJ}$  are hydraulic conductivity in Table 3. We selected the scaling values for  $k_{xx}$  and  $k_{yy}$  to achieve a similar range of displacements between the scenarios, making comparison easier. The hydraulic conductivity in the  $z$  direction remains constant across all scenarios.

These simulations show distinct patterns in surface displacement. The IHC scenario exhibits circular surface displacements. In contrast,

the AHC simulations demonstrate elliptical surface displacement and the higher the anisotropy ratio the more pronounced the elliptical shape becomes.

### 6.3. Possibility of using InSAR to determine AHC in aquifers

We now aim to ascertain whether the surface displacement resulting from our model of the Anderson Junction aquifer pumping test can be detected using InSAR. We also explore the scenarios of higher pumping rates and/or a longer duration of pumping to understand if such a pumping test could lead to observable surface displacements with InSAR.

As explained in Section 4, successful detection of surface displacement using Sentinel-1 InSAR requires displacements exceeding 8 mm along the LOS within a specific region around the well, e.g. an elliptical displacement pattern that demonstrates AHC. Fig. 9 illustrates the surface displacement along line  $xx'$  and  $yy'$  at various time points. It is evident that the maximum surface displacement is only 3 mm. Consequently, under our conceptual model assumptions, the magnitude of the surface displacements created during the original Anderson Junction test described in Heilweil and Hsieh (2006) was likely insufficient to be detected by Sentinel-1 InSAR.

Despite this negative result, the model gives us a tool to explore under which scenarios a future test at Anderson Junction could produce a sufficient response detectable by InSAR and contain valuable information for inferring AHC. To this end, we explored three alternative scenarios. For reference in the following discussion, the LOS surface displacement under the original Anderson Junction test conditions is shown in Fig. 7.

In the first scenario, *high pumping rate*, shown in Fig. 10a we increase the pumping rate to eight times the value used in the original Anderson Junction test, while keeping the pumping duration fixed. The maximum line of sight displacement increased to 18 mm (detectable by InSAR), and the displacement pattern has a strong elliptical character.

In the second scenario, *long pumping duration*, shown in Fig. 10b, we increase the pumping time to 32d and keep the pumping rate the same as that used in the original Anderson Junction test. The maximum line of sight displacement is significantly lower than the first scenario at 8.6 mm, although still potentially at the threshold for detection by Sentinel-1 InSAR. Additionally, the longer pumping has led to a significantly more diffuse and isotropic displacement response than in the high pumping rate scenario. This can be attributed to the longer pumping having sufficient time to activate the slower diffusion timescale of the fluid problem along the minor axis  $Y$ .



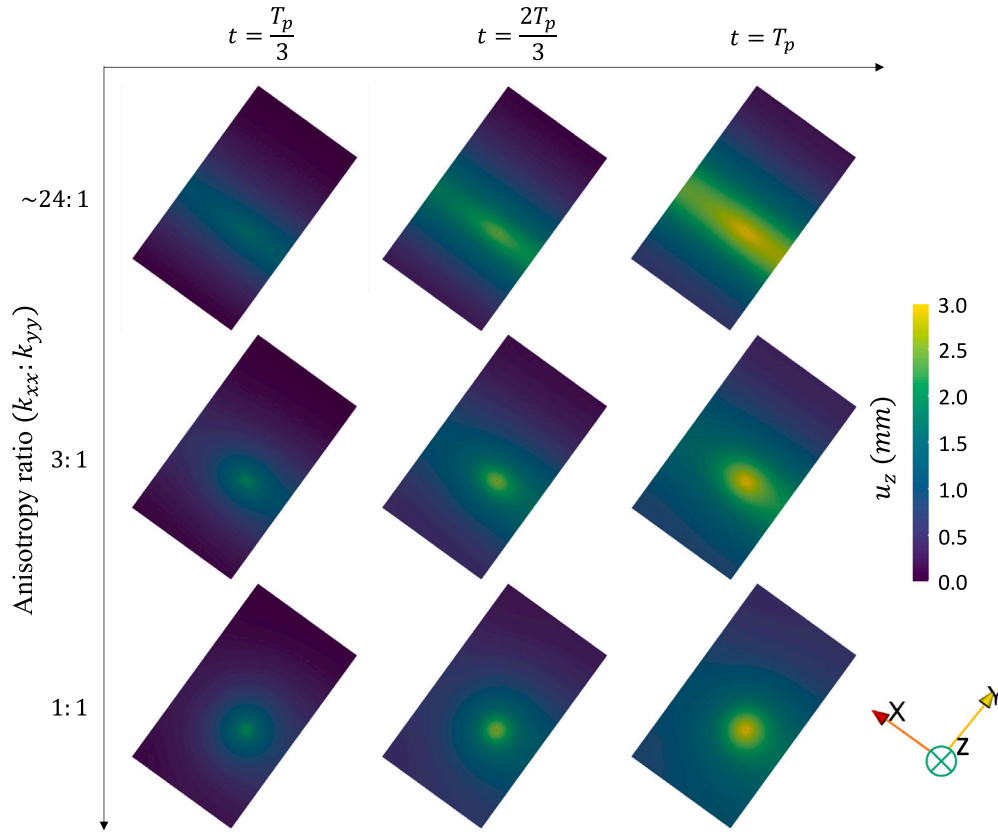


Fig. 8. Surface displacements for three simulated scenarios: IHC, AHC with a 3:1 anisotropy ratio, and AHC with an anisotropy ratio of approximately 24:1. The images display the surface displacements at three times during the pumping phase.

Finally, we show an *intermediate rate and duration* scenario, shown in Fig. 10c with eight days of pumping and four times the pumping rate of the original Anderson Junction test. This scenario is a compromise between the high pumping rate scenario Fig. 10a and the long pumping rate scenario Fig. 10b. We can see that a strong elliptical LOS displacement pattern is visible and that the maximum displacement at 13.3 mm exceeds the threshold for detection by Sentinel-1 InSAR. Note that by design the total water extracted

$$Q = \int_0^{T_p} \int_{\Gamma_{pw}} g_p \, dx \, dt, \quad (5)$$

is the same in the three scenarios.

Fig. 11 presents a comparison of LOS surface displacement for the different scenarios along line  $xx'$  and  $yy'$ . Notably, the graph shows that along line  $yy'$ , the high pumping rate causes substantial surface displacement gradients around the pumping well, which could result in sinking and fissure formation (Galloway et al., 1999, p. 132–133) (although, our model cannot predict this type of localized process directly).

We conclude that in terms of maximizing the potential information content with respect to inferring possible anisotropy, it is important to strongly perturb the system via the pumping rate to ensure that the anisotropic character is visible *and* to pump a sufficient volume of water such that the LOS surface displacement can be detected by the chosen InSAR technology. However, it is important to note that there are practical limitations to how much we can increase the pumping rate or pumping duration, as they must align with the aquifer's properties, sustainability considerations and engineering considerations, see e.g. Osborne (1993) for a discussion.

#### 6.4. The required aquifer test features for using SAR data

In assessing the potential utility of SAR data for studying an aquifer system undergoing an aquifer test, several key considerations need to

be taken into account, including the availability of data, the temporal resolution of SAR mission and accuracy of surface displacement measurements. The temporal resolution of the SAR data is important in case of acquiring more SAR data around the aquifer test time. We need at least one suitable pair of InSAR data within the aquifer test interval like in Alghamdi (2020) study, although having multiple data points within a longer test interval can enhance the understanding of the aquifer system. Moreover, it is crucial to assess whether the surface displacement caused by the aquifer test is observable through InSAR techniques. Therefore this is one of our motivations to build the proposed model to predict the surface displacement in the Anderson Junction aquifer.

In summary, to ensure the feasibility of using SAR data to estimate anisotropic aquifer properties, four key considerations should be taken into account when designing the aquifer test:

1. Availability of SAR data: It is essential to confirm the availability of SAR datasets specifically for the time and location of the aquifer test.
2. Adequate test interval: The aquifer test should have a sufficiently long time interval. This allows for the collection of multiple SAR data sets, enabling a more comprehensive study of the aquifer over time.
3. Sufficient total water extraction to ensure high LOS displacement: The observed LOS displacement should exceed a minimum threshold, e.g. 8 mm or more for the Sentinel-1 mission (Cigna et al., 2021).
4. A sufficiently high pumping rate to activate anisotropic behavior: to ensure a elliptical displacement response driven by the activation of the flow on the major principal axis vs the minor principal axis.

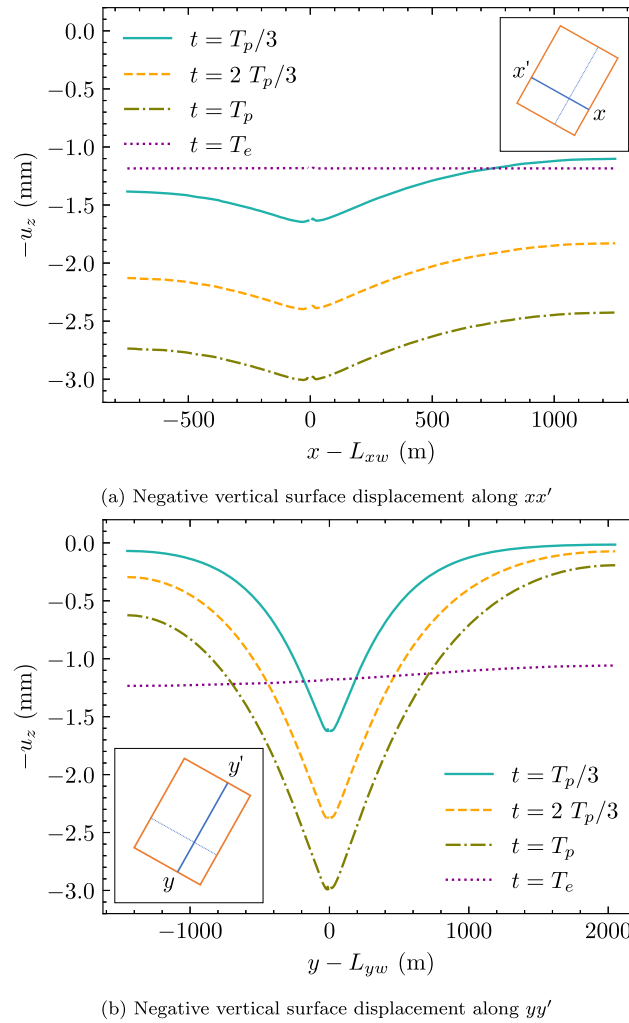


**Fig. 9.** Negative vertical surface displacement along line  $xx'$  and line  $yy'$  at different time points. The maximum predicted surface displacement during the pump test reaches 3 mm.

## 7. Conclusions

We have developed an anisotropic poroelastic finite element model of the Anderson Junction site that is capable of predicting coupled fluid flow and displacements. Our results show that the effective elastic response of the aquifer at the Earth's surface has an anisotropic nature driven by the underlying anisotropy in the fluid problem, even when the elasticity problem is assumed to be isotropic. In the LOS displacement, this anisotropy manifests as distinctive elliptical patterns.

Under our model assumptions, the original Anderson Junction aquifer test described in Heilweil and Hsieh (2006) probably did not exhibit sufficient surface displacement for detection using InSAR. In three alternative scenarios, we explored longer pumping and/or higher pumping rates to explore the potential of using InSAR data to calibrate aquifer models with AHC – in two of these scenarios, see Fig. 10a and Fig. 10c, we predict LOS displacement levels necessary for detection by the contemporary Sentinel-1 InSAR mission. We add that the proposed model can be adapted to another aquifer test with a longer pumping and/or higher pumping rate or another confined aquifer system by changing the properties of the aquifer. It is also recommended to conduct extended pumping duration to gather InSAR data from multiple satellite passes.

Our upcoming research will explore two directions. First, due to uncertainty in the hydraulic conductivity tensor, we want to develop a stochastic model of AHC that respects the underlying material symmetries, e.g. Cowin and Doty (2007, Chapter 5). Second, with this

stochastic model developed, we plan to assimilate InSAR-derived data into our aquifer model. This entails collecting field and remote sensing data to assess aquifer discharge and recharge dynamics. InSAR will offer valuable insights into surface displacement and underlying aquifer structures. By solving the inverse problem using spatiotemporal data, we aim to estimate aquifer properties following e.g. Alghamdi et al. (2020, 2021). These investigations promise to significantly advance our understanding of aquifers with AHC behavior leading to models with improved predictive power for use in a groundwater management context.

## Acronyms

AHC	anisotropic hydraulic conductivity
FEM	Finite Element Method
GNSS	Global Navigation Satellite System
GPS	Global Positioning System
IHC	isotropic hydraulic conductivity
InSAR	Interferometric Synthetic Aperture Radar
LOS	Line of Sight
SAR	Synthetic Aperture Radar
USGS	US Geological Survey

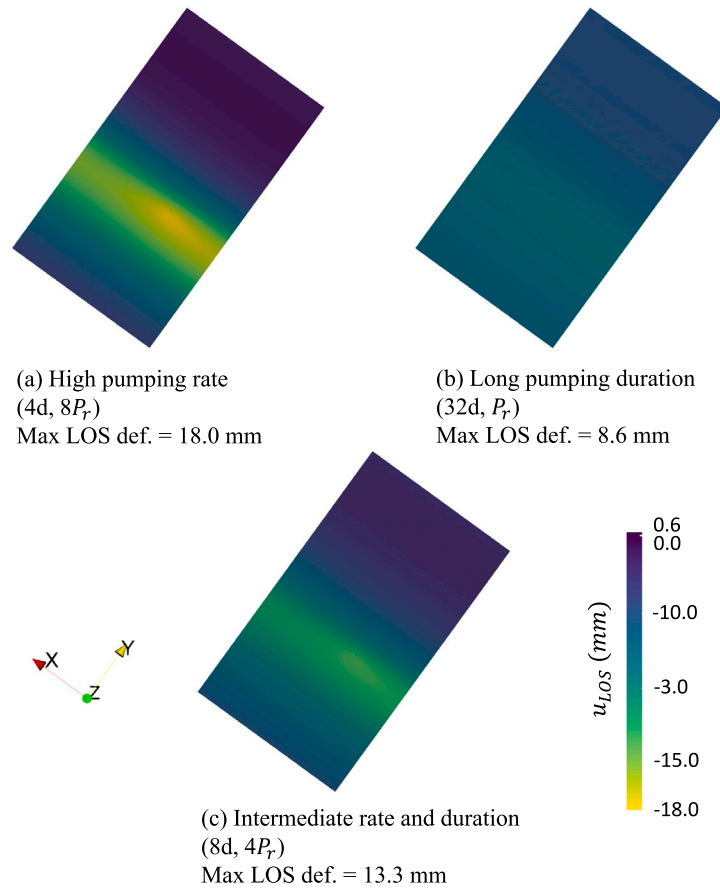


**Fig. 10.** Simulated LOS surface displacement at the end of pumping for: (a) an 8 times pumping rate compared to the Anderson Junction test. (b) an extended pumping duration of 32 d, replicating the aquifer test characteristics of Anderson Junction (c) an extended intermediate pumping with 4 times rate and 8 d duration. In all cases, the total volume of extracted groundwater is the same. Note the different colorbar scale to Fig. 7.

#### CRediT authorship contribution statement

**Sona Salehian Ghamsari:** Writing – original draft, Visualization, Validation, Software, Methodology, Investigation, Formal analysis, Data curation. **Tonie van Dam:** Writing – review & editing, Supervision, Funding acquisition, Conceptualization. **Jack S. Hale:** Writing – review & editing, Supervision, Software, Project administration, Methodology, Investigation, Funding acquisition, Conceptualization.

#### Code availability section

AHC-Poroelastic-Model  
Contact: [salehiyan.sona@gmail.com](mailto:salehiyan.sona@gmail.com).  
Hardware requirements: x86-64 or ARM computer with container runtime e.g. Docker.  
Program language: Python  
Software required: Python, Paraview with Python interface (pypython), Docker, DOLFINx.  
The source code and Docker image are available for download at <https://github.com/sonasehian/ahc-poroelastic-model> and at Salehian Ghamsari and Hale (2024).

#### Funding

This work was funded in whole, or in part, by the Luxembourg National Research Fund (FNR), grant reference PRIDE/17/12252781. For the purposes of open access, and in fulfillment of the obligations arising from the grant agreement, the authors have applied a Creative Commons Attribution 4.0 International (CC BY 4.0) license to any Author Accepted Manuscript version arising from this submission.

#### Declaration of competing interest

The authors declare that they have no known competing financial interests or personal relationships that could have appeared to influence the work reported in this paper.

#### Acknowledgments

We would like to thank Natascha Kuhlmann from the University of Bonn for her assistance in interpreting the geologic maps and providing insights into the geological characteristics of the study area. We would also like to thank Hamid Dehghani from the Luxembourg Institute of Science and Technology (LIST) for his guidance selecting appropriate poroelastic constants.

#### Appendix A. Finite element discretization of Biot's poroelasticity model

In this appendix, we recall the three-field FEM discretization of Biot's theory which broadly follows the original development in Ferronato et al. (2010).

##### A.1. Notation

We recall the aquifer problem domain  $\Omega \subset \mathbb{R}^3$  and its boundary  $\Gamma$  with outwards pointing normal  $n$ . For any subset  $\omega$  of  $\bar{\Omega} := \Omega \cup \Gamma$  we denote  $L^2(\omega)$  as the usual Sobolev space of square integrable functions

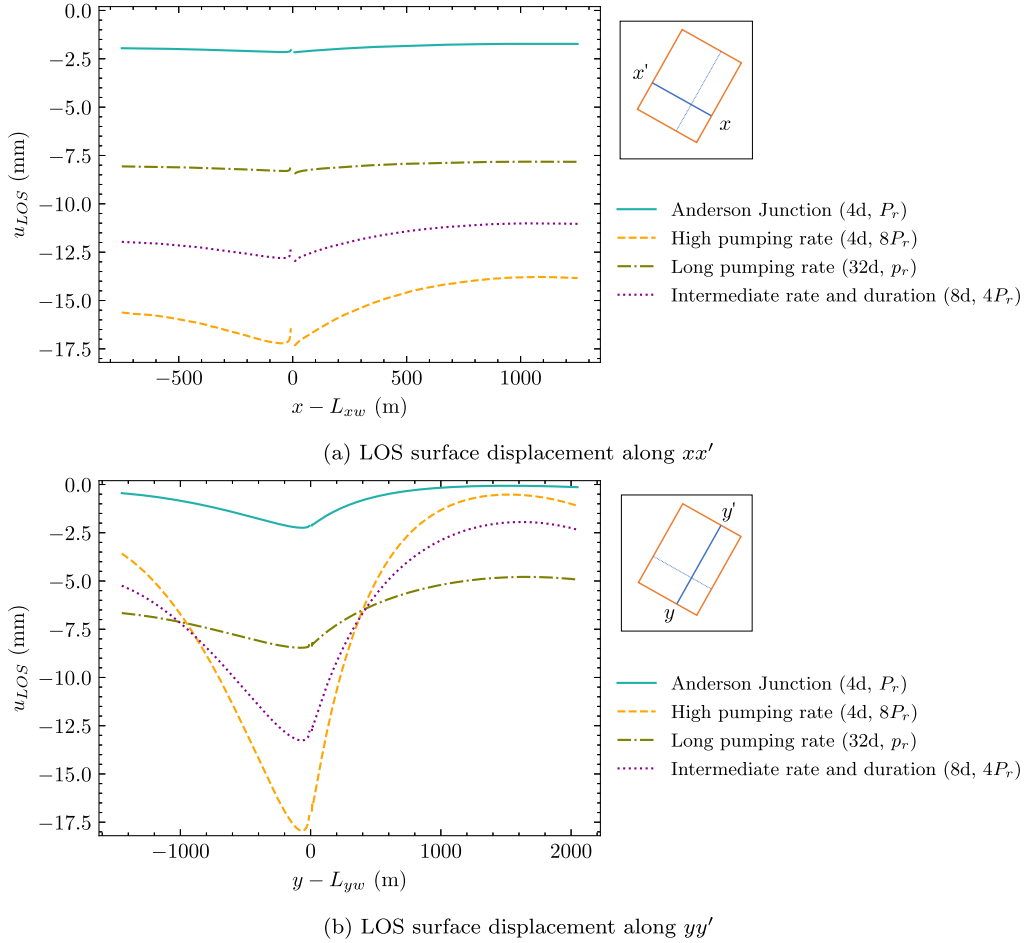


**Fig. 11.** Comparison of LOS surface displacement along line  $xx'$  and line  $yy'$  at the end of pumping ( $T_p$ ) for different pumping scenarios. Along  $yy'$ , excessive pumping leads to a significant surface displacement gradient, which could lead to sinking and the formation of fissures near the pumping well (Galloway et al., 1999, p. 132–133).

on  $\omega$ , and  $(\cdot, \cdot)_\omega$  the associated inner product, which for two arguments  $f, g \in L^2(\omega)$  can be written

$$(f, g)_{L^2(\omega)} = \int_\omega f g \, dx. \quad (\text{A.1})$$

For brevity, we introduce the compact notation  $(\cdot, \cdot)_\omega := (\cdot, \cdot)_{L^2(\omega)}$  and  $(\cdot, \cdot) := (\cdot, \cdot)_{L^2(\Omega)}$ . We can similarly denote  $H^1(\omega)$  as the usual Sobolev space of square integrable functions with weak derivatives in  $L^2(\omega)$  with associated inner product  $(\cdot, \cdot)_{H^1(\omega)}$  defined as

$$(f, g)_{H^1(\omega)} = \int_\omega f g + \nabla f \nabla g \, dx, \quad (\text{A.2})$$

where  $\nabla$  is the usual gradient of a scalar function.

Finally, we introduce the slightly less standard Sobolev space  $H(\text{div}; \omega)$  as the space of Sobolev space of vector-valued square integrable functions with square integrable divergence on  $\omega$

$$H(\text{div}; \Omega) = \{f : f \in (L^2(\Omega))^3, \text{div } f \in L^2(\Omega)\}, \quad (\text{A.3})$$

where the  $\text{div}$  operator is acting on a vector-valued function  $f$  with components  $(f_1, f_2, f_3)$  can be written as

$$\text{div } f := \nabla \cdot f := \frac{\partial f_1}{\partial x_1} + \frac{\partial f_2}{\partial x_2} + \frac{\partial f_3}{\partial x_3}. \quad (\text{A.4})$$

## A.2. Weak formulation

We briefly recall the strong form of the three-field formulation of Biot's equations that was outlined in section 3.1. Given a domain  $\Omega \subset$

$\mathbb{R}^3$  with boundary  $\Gamma$  find the fluid-pore pressure  $p : \Omega \times (0, T] \rightarrow \mathbb{R}$ , deformation  $u : \Omega \times (0, T] \rightarrow \mathbb{R}^3$  and fluid flux  $q : \Omega \times (0, T] \rightarrow \mathbb{R}^3$  such that

$$(S_\epsilon p + \alpha \nabla \cdot u)_t + \nabla \cdot q = f_p \text{ in } \Omega \times (0, T], \quad (\text{A.5a})$$

$$-\nabla \cdot \bar{\sigma} = f_u \text{ in } \Omega \times (0, T], \quad (\text{A.5b})$$

$$q + k \nabla p = 0 \text{ in } \Omega \times (0, T], \quad (\text{A.5c})$$

with boundary conditions

$$u = u_d \text{ on } \Gamma_u^d \times (0, T], \quad (\text{A.5d})$$

$$\bar{\sigma} \cdot n = g_u \text{ on } \Gamma_u^n \times (0, T], \quad (\text{A.5e})$$

$$p = p_d \text{ on } \Gamma_p^d \times (0, T], \quad (\text{A.5f})$$

$$q \cdot n = g_p \text{ on } \Gamma_p^n \times (0, T], \quad (\text{A.5g})$$

where the boundary  $\Gamma$  has been partitioned into disjoint parts for both the solid problem  $\Gamma = \Gamma_u^d \cup \Gamma_p^n$  and the fluid problem  $\Gamma = \Gamma_p^d \cup \Gamma_u^n$  and initial conditions

$$p(x, 0) = p^0 \text{ on } \Omega, \quad (\text{A.5h})$$

$$u(x, 0) = u^0 \text{ on } \Omega, \quad (\text{A.5i})$$

$$q(x, 0) = q^0 \text{ on } \Omega, \quad (\text{A.5j})$$

To simplify what follows, but without loss of generality, we make the following regularity assumptions in space for the pressure

$$\mathcal{P} = \{p : \Omega \times [0, T] \rightarrow \mathbb{R} \mid p \in L^2(\Omega)\}, \quad (\text{A.6a})$$



$$\mathcal{U} = \{u : \Omega \times [0, T] \rightarrow \mathbb{R}^3 \mid u \in (H^1(\Omega))^3, u = u_d \text{ on } \Gamma_u^d\}, \quad (\text{A.6b})$$

$$\mathcal{Q} = \{q : \Omega \times [0, T] \rightarrow \mathbb{R}^3 \mid q \in H(\text{div}; \Omega), q \cdot n = g_p \text{ on } \Gamma_p^n\}. \quad (\text{A.6c})$$

Additional sufficient regularity assumptions in time are also required, which we ignore for simplicity.

To derive the weak form of the system Eq. (A.5), we multiply Eqs. (A.5a)–(A.5c) by test functions  $\tilde{p} \in \mathcal{P}$ ,  $\tilde{u} \in \mathcal{U}_0$ , and  $\tilde{q} \in \mathcal{Q}_0$ , respectively, where

$$\mathcal{U}_0 = \{u \in \mathcal{U} \mid u_d = 0\}, \quad (\text{A.7a})$$

$$\mathcal{Q}_0 = \{q \in \mathcal{Q} \mid g = 0\}, \quad (\text{A.7b})$$

and then integrate over the domain  $\Omega$  before applying any necessary integration by parts results.

Starting this process with Eq. (A.5a) we straightforwardly obtain

$$((S_e p + \alpha \nabla \cdot u)_t, \tilde{p})_\Omega + (\nabla \cdot q, \tilde{p})_\Omega = (f_p, \tilde{p})_\Omega, \quad \forall \tilde{p} \in \mathcal{P}. \quad (\text{A.8})$$

Continuing with Eq. (A.5b), we obtain

$$(-\nabla \cdot \tilde{\sigma}, \tilde{u})_\Omega = (f, \tilde{u})_\Omega \quad \forall \tilde{u} \in \mathcal{U}_0, \quad (\text{A.9})$$

and then using integration by parts gives for all  $\tilde{u} \in \mathcal{U}_0$

$$(\nabla \cdot \tilde{\sigma}, \tilde{u})_\Omega = -(\tilde{\sigma}, \nabla \tilde{u})_\Omega + (\tilde{\sigma} n, \tilde{u})_\Gamma \quad \forall \tilde{u} \in \mathcal{U}_0. \quad (\text{A.10})$$

Splitting the integral on the boundary into its two constituent parts

$$(\tilde{\sigma} n, \tilde{u})_\Gamma = (\tilde{\sigma} n, \tilde{u})_{\Gamma_u^d} + (\tilde{\sigma} n, \tilde{u})_{\Gamma_u^n}, \quad (\text{A.11})$$

and, using the definition of the space  $\mathcal{U}_0$  and the knowledge that  $\tilde{\sigma} n = g_u$  on  $\Gamma_u^n$ , allows us to write

$$(\tilde{\sigma}, \nabla \tilde{u})_\Omega = (f, \tilde{u})_\Omega + (g_u, \tilde{u})_{\Gamma_u^n}, \quad \forall \tilde{u} \in \mathcal{U}_0. \quad (\text{A.12})$$

Finally, for equation (A.5c) we obtain

$$(\nabla p, \tilde{q})_\Omega = -(k^{-1} q, \tilde{q})_\Omega, \quad \forall \tilde{q} \in \mathcal{Q}_0, \quad (\text{A.13})$$

where  $k^{-1}$  denotes the inverse of  $k$ , and applying integration by parts on the term on the left hand side of Eq. (A.13) gives

$$-(\nabla \cdot \tilde{q}, p)_\Omega + (p, \tilde{q} \cdot n)_\Gamma = -(k^{-1} q, \tilde{q}), \quad \forall \tilde{q} \in \mathcal{Q}_0. \quad (\text{A.14})$$

Splitting the integral on the boundary into its two constituent parts

$$(p, \tilde{q} \cdot n)_\Gamma = (p, \tilde{q} \cdot n)_{\Gamma_p^d} + (p, \tilde{q} \cdot n)_{\Gamma_p^n}, \quad (\text{A.15})$$

and using the definition of the space  $\mathcal{Q}_0$  and the knowledge that  $q \cdot n = g$  on  $\Gamma_p^n$

$$-(k^{-1} q, \tilde{q})_\Omega + (p, \nabla \cdot \tilde{q})_\Omega = (p_d, \tilde{q} \cdot n)_{\Gamma_p^d}, \quad \forall \tilde{q} \in \mathcal{Q}_0. \quad (\text{A.16})$$

In summary, the final variational problem is to find  $p \in \mathcal{P}$ ,  $u \in \mathcal{U}$ , and  $q \in \mathcal{Q}$  that satisfy the equations

$$((S_e p + \alpha \nabla \cdot u)_t, \tilde{p})_\Omega + (\nabla \cdot q, \tilde{p})_\Omega = (f_p, \tilde{p})_\Omega, \quad (\text{A.17a})$$

$$(\tilde{\sigma}(u, p), \nabla \tilde{u})_\Omega = (f, \tilde{u})_\Omega + (g_u, \tilde{u})_{\Gamma_u^n}, \quad (\text{A.17b})$$

$$-(k^{-1} q, \tilde{q})_\Omega + (p, \nabla \cdot \tilde{q})_\Omega = (p_d, \tilde{q} \cdot n)_{\Gamma_p^d}. \quad (\text{A.17c})$$

for all test functions  $\tilde{p} \in \mathcal{P}$ ,  $\tilde{u} \in \mathcal{U}_0$ , and  $\tilde{q} \in \mathcal{Q}_0$ . We emphasize that in this three-field formulation the flux boundary condition Eq. (A.5g) is built strongly into the space  $\mathcal{Q}$  and the pressure boundary condition Eq. (A.5f) occurs weakly in Eq. (A.17c). By contrast, in the classical two-field formulation the flux boundary condition occurs weakly and the pressure boundary condition is built strongly into a space  $\mathcal{P}$  with stronger  $H^1$ -regularity requirements.

### A.3. Discretization in time

For discretizing Eq. (A.17) in time, we use a first-order backwards Euler method, see e.g. Langtangen and Logg (2016) for full details.

Consider  $M + 1$  time steps  $0 = t^0 < t^1 < t^2 < \dots < t^M = T$  uniformly spaced on the interval  $[0, T]$  giving a constant timestep  $\Delta t = \Delta t^n =$

$t^{n+1} - t^n$  for  $n \in 0, \dots, M - 1$ . The first-order backwards Euler scheme approximates the time derivative on the displacement  $u$  and pressure  $p$  as

$$(p^{n+1})_t \approx \frac{p^{n+1} - p^n}{\Delta t}, \quad \forall n \in 0, \dots, M - 1, \quad (\text{A.18a})$$

$$(u^{n+1})_t \approx \frac{u^{n+1} - u^n}{\Delta t}, \quad \forall n \in 0, \dots, M - 1. \quad (\text{A.18b})$$

Following standard arguments, and after some minor rearrangements, the discrete time version of Eq. (A.17) can be written: For  $n = 0, \dots, M - 1$  find  $p^{n+1} \in \mathcal{P}$ ,  $u^{n+1} \in \mathcal{U}$ , and  $q^{n+1} \in \mathcal{Q}$  such that

$$(S_e p^{n+1} + \alpha \nabla \cdot u^{n+1} + \Delta t \nabla \cdot q^{n+1}, \tilde{p}) = (\Delta t f_p^{n+1} + S_e p^n + \alpha \nabla \cdot u^n, \tilde{p}), \quad (\text{A.19a})$$

$$-(\tilde{\sigma}(u^{n+1}, p^{n+1}), \nabla \tilde{u}) = -(f_u^{n+1}, \tilde{u}) - (g_u^{n+1}, \tilde{u})_{\Gamma_u^n}, \quad (\text{A.19b})$$

$$-(\Delta t k^{-1} q^{n+1}, \tilde{q}) + (\Delta t p^{n+1}, \nabla \cdot \tilde{q}) = (\Delta t p_d^{n+1}, \tilde{q} \cdot n)_{\Gamma_p^d}, \quad (\text{A.19c})$$

for all test functions  $\tilde{p} \in \mathcal{P}$ ,  $\tilde{u} \in \mathcal{U}_0$ , and  $\tilde{q} \in \mathcal{Q}_0$ . Note that Eq. (A.19c) has been multiplied by  $\Delta t$  to maintain symmetry with the term  $(\Delta t \nabla \cdot q^{n+1}, \tilde{p})$  in Eq. (A.19a).

### A.4. Discretization in space

For spatial discretization, we employ the mass-conservative three-field finite element formulation (Ferronato et al., 2010) ensuring conservation of mass within the numerical model. The implementation of the finite element formulation (Brenner and Scott, 2008) was carried out using DOLFINx, a finite element computing library (Baratta et al., 2023).

We are guided by Ferronato et al. (2010), Haugen et al. (2020) in choosing finite element spaces in which the field variables  $p$ ,  $u$  and  $q$  are approximated. Specifically, we approximate the pressure  $p_h \in \mathcal{P}_h \subset \mathcal{P}$  by zero-order discontinuous Lagrange finite elements, the displacements  $u_h \in \mathcal{U}_h \subset \mathcal{U}$  vector-valued first-order continuous Lagrange finite elements, and the flux  $q_h \in \mathcal{Q}_h \subset \mathcal{Q}$  the vector-valued Brezzi–Douglas–Marini (BDM) elements (Brezzi et al., 1985) of lowest order which naturally discretize  $H(\text{div}; \Omega)$ . This formulation is known to be inf-sup stable according to the stability theory of finite element methods (Brenner and Scott, 2008), to guarantee discrete mass conservation (Ferronato et al., 2010), and to be free from spurious pressure oscillations that can cause numerical issues in two-field pressure-displacement formulations of Biot's theory (Ferronato et al., 2010). We note that Ferronato et al. (2010), Alghamdi (2020) use a lowest-order Raviart–Thomas (RT) type space for the flux which has slightly weaker interpolation results than the BDM space used here.

### A.5. Enforcing no normal displacement at the well boundary

We briefly describe the method by which we enforce the boundary condition on the normal component of the displacement  $u \cdot n = 0$  on the well surface  $\Gamma_w$  as specified in Table 4. This boundary condition is recommended as being the most physically justifiable choice in Burbey (2006). By contrast, Alghamdi (2020) did not explicitly include the well surface in their model, instead choosing to model the extraction as a volume forcing using  $f_p$ .

Instead of building the boundary condition  $u \cdot n = 0$  strongly into the space  $\mathcal{U}$ , we choose to enforce it weakly using a penalty-free non-symmetric Nitsche-type method proposed in Chouly et al. (2015). Our decision to enforce this condition weakly was made largely to ease the implementation in DOLFINx, where imposing boundary conditions of type  $u \cdot n = 0$  strongly in the space is not straightforward.

For simplicity we did not include this more complex boundary condition when developing Eq. (A.19), instead choosing to enforce this

by a modification to Eq. (A.19b) here. Following Chouly et al. (2015) we add two terms on the left-hand side of Eq. (A.19b)

$$\begin{aligned} & -(\bar{\sigma}(u^{n+1}, p^{n+1}), \nabla \bar{u}) \\ & -(\bar{\sigma}(u^{n+1}, p^{n+1}) \cdot n, \bar{u} \cdot n)_{\Gamma_w} + (\bar{\sigma}(\bar{u}^{n+1}, \bar{p}^{n+1}) \cdot n, u \cdot n)_{\Gamma_w} \\ & = -(\bar{f}_u^{n+1}, \bar{u}) - (\bar{g}_u^{n+1}, \bar{u})_{\Gamma_u^n}, \quad \forall \bar{p} \in P_0, \forall q \in Q_0. \end{aligned} \quad (\text{A.20})$$

that weakly enforce the condition  $u \cdot n = 0$  on  $\Gamma_w$ .

#### A.6. Mesh generation

The geometry of the model was meshed using gmsh (Geuzaine and Remacle, 2009) for finite element analysis. The resulting 3D mesh conforms to the aquifer system's three layers. The element size varies from 6 to 40 m, and the total number of the elements is 368329. The mesh incorporates different element sizes at different locations and in different layers, this will ensure an appropriate resolution that will improve the accuracy of the model. As we approach the well, the mesh elements become finer, enabling us to the capture of localized effects with lower error.

### Appendix B. Supplementary material

The supplementary material (Salehian Ghamsari and Hale, 2024) includes code, input data and mathematical details of the finite element solver alongside a Docker container to execute the code in. We have also included a video version of Fig. 7 showing the deformation of the Anderson Junction simulation.

#### Data availability

Supplementary material for “Can the anisotropic hydraulic conductivity of an aquifer be determined using surface displacement data? A case study” (Zenodo)

### References

- Alghamdi, A., 2020. Bayesian Inverse Problems for Quasi-Static Poroelasticity with Application to Ground Water Aquifer Characterization from Geodetic Data (Ph.D. thesis). University of Texas at Austin, <http://dx.doi.org/10.26153/tsw/13182>.
- Alghamdi, A., Hesse, M.A., Chen, J., Ghattas, O., 2020. Bayesian poroelastic aquifer characterization from InSAR surface deformation data. Part I: Maximum a posteriori estimate. *Water Resour. Res.* 56 (10), <http://dx.doi.org/10.1029/2020WR027391>, e2020WR027391.
- Alghamdi, A., Hesse, M.A., Chen, J., Villa, U., Ghattas, O., 2021. Bayesian poroelastic aquifer characterization from InSAR surface deformation data. 2. Quantifying the uncertainty. *Water Resour. Res.* 57 (11), <http://dx.doi.org/10.1029/2021WR029775>, e2021WR029775.
- Amitrano, D., Martino, G.D., Iodice, A., Mitidieri, F., Papa, M.N., Riccio, D., Ruello, G., 2014. Sentinel-1 for monitoring reservoirs: A performance analysis. *Remote Sens.* 6 (11), 10676–10693. <http://dx.doi.org/10.3390/rs61110676>.
- Baratta, I.A., Dean, J.P., Dokken, J.S., Habera, M., Hale, J.S., Richardson, C.N., Rognes, M.E., Scroggs, M.W., Sime, N., Wells, G.N., 2023. DOLFINX: The next generation FEniCS problem solving environment. <http://dx.doi.org/10.5281/zenodo.10447666>, Zenodo.
- Basu, N.B., Van Meter, K., 2014. 4.3 - Sustainability of groundwater resources. In: Ahuja, S. (Ed.), *Comprehensive Water Quality and Purification*. Elsevier, Waltham, pp. 57–75. <http://dx.doi.org/10.1016/B978-0-12-382182-9.00062-1>.
- Batzle, M., Duranti, L., Rector, J., Pride, S., 2007. Measurement and Interpretation of Seismic Attenuation for Hydrocarbon Exploration. Technical Report, Colorado School of Mines, Golden, CO (United States), <http://dx.doi.org/10.2172/927592>.
- Berre, I., Doster, F., Keilegavlen, E., 2019. Flow in fractured porous media: A review of conceptual models and discretization approaches. *Transp. Porous Media* 130 (1), 215–236. <http://dx.doi.org/10.1007/s11242-018-1171-6>.
- Biot, M.A., 1941. General theory of three-dimensional consolidation. *J. Appl. Phys.* 12 (2), 155–164. <http://dx.doi.org/10.1063/1.1712886>.
- Boni, R., Cigna, F., Bricker, S., Meisina, C., McCormack, H., 2016. Characterisation of hydraulic head changes and aquifer properties in the London basin using persistent scatterer interferometry ground motion data. *J. Hydrol.* 540, 835–849. <http://dx.doi.org/10.1016/j.jhydrol.2016.06.068>.
- Boni, R., Meisina, C., Cigna, F., Herrera, G., Notti, D., Bricker, S., McCormack, H., Tomás, R., Béjar-Pizarro, M., Mulas, J., Ezquerro, P., 2017. Exploitation of satellite A-DInSAR time series for detection, characterization and modelling of land subsidence. *Geosciences* 7 (2), <http://dx.doi.org/10.3390/geosciences7020025>.
- Brenner, S.C., Scott, L.R., 2008. The mathematical theory of finite element methods. In: Marsden, J.E., Sirovich, L., Antman, S.S. (Eds.), *Texts in Applied Mathematics*, vol. 15, Springer, New York, NY, <http://dx.doi.org/10.1007/978-0-387-75934-0>.
- Brezzi, F., Douglas, J., Marini, L.D., 1985. Two families of mixed finite elements for second order elliptic problems. *Numer. Math.* 47, 217–235. <http://dx.doi.org/10.1007/BF01389710>.
- Burbey, T.J., 2006. Three-dimensional deformation and strain induced by municipal pumping, part 2: Numerical analysis. *J. Hydrol.* 330 (3), 422–434. <http://dx.doi.org/10.1016/j.jhydrol.2006.03.035>.
- Burbey, T.J., Warner, S.M., Blewitt, G., Bell, J.W., Hill, E., 2006. Three-dimensional deformation and strain induced by municipal pumping, part 1: Analysis of field data. *J. Hydrol.* 319 (1), 123–142. <http://dx.doi.org/10.1016/j.jhydrol.2005.06.028>.
- Caretta, M., Mukherji, A., Arfanuzzaman, M., Betts, R., Gelfan, A., Hirabayashi, Y., Lissner, T., Liu, J., Gunn, E.L., Morgan, R., Mwanga, S., Supratid, S., 2022. Water. In: *Climate change 2022: Impacts, adaptation and vulnerability*. In: Pörtner, H.-O., Roberts, D., Tignor, M., Poloczanska, E., Mintenbeck, K., Alegría, A., Craig, M., Langsdorf, S., Löschke, S., Möller, V., Okem, A., Rama, B. (Eds.), Cambridge University Press, Cambridge, UK and New York, NY, USA, pp. 551–712. <http://dx.doi.org/10.1017/9781009325844.006>.
- Chaussard, E., Bürgmann, R., Shirzaei, M., Fielding, E.J., Baker, B., 2014. Predictability of hydraulic head changes and characterization of aquifer-system and fault properties from InSAR-derived ground deformation. *J. Geophys. Res.: Solid Earth* 119 (8), 6572–6590. <http://dx.doi.org/10.1002/2014JB011266>.
- Cheng, C.H., Toksöz, M.N., 1979. Inversion of seismic velocities for the pore aspect ratio spectrum of a rock. *J. Geophys. Res.: Solid Earth* 84 (B13), 7533–7543. <http://dx.doi.org/10.1029/JB084iB13p07533>.
- Chouly, F., Hild, P., Renard, Y., 2015. Symmetric and non-symmetric variants of Nitsche's method for contact problems in elasticity: theory and numerical experiments. *Math. Comp.* 84 (293), 1089–1112. <http://dx.doi.org/10.1090/S0025-5718-2014-02913-X>.
- Cigna, F., Esquivel Ramírez, R., Tapete, D., 2021. Accuracy of sentinel-1 PSI and SBAS InSAR displacement velocities against GNSS and geodetic leveling monitoring data. *Remote Sens.* 13 (23), <http://dx.doi.org/10.3390/rs13234800>.
- Cowin, S.C., Doty, S.B., 2007. *Tissue Mechanics*. Springer, <http://dx.doi.org/10.1007/978-0-387-49985-7>.
- Dehghani, H., Penta, R., Merodio, J., 2018. The role of porosity and solid matrix compressibility on the mechanical behavior of poroelastic tissues. *Mater. Res. Express* 6 (3), 035404. <http://dx.doi.org/10.1088/2053-1591/aaf5b9>.
- Duan, W., Zhang, H., Wang, C., Tang, Y., 2020. Multi-temporal InSAR parallel processing for sentinel-1 large-scale surface deformation mapping. *Remote Sens.* 12 (22), <http://dx.doi.org/10.3390/rs12223749>.
- Earle, S., 2019. 14.1 groundwater and aquifers. URL: <https://opentextbc.ca/physicalgeology2ed/chapter/14-1-groundwater-and-aquifers/>.
- Erkens, G., Bucx, T., Dam, R., de Lange, G., Lambert, J., 2015. Sinking coastal cities. *Proc. Int. Assoc. Hydrol. Sci.* 372, 189–198. <http://dx.doi.org/10.5194/piahs-372-189-2015>.
- European Space Agency (ESA), 2023. User guides - Sentinel-1 SAR - Interferometric wide swath - Sentinel online. URL: <https://sentinels.copernicus.eu/web/sentinel/user-guides>.
- Famiglietti, J.S., Lo, M., Ho, S.L., Bethune, J., Anderson, K.J., Syed, T.H., Swenson, S.C., de Linage, C.R., Rodell, M., 2011. Satellites measure recent rates of groundwater depletion in California's Central Valley. *Geophys. Res. Lett.* 38 (3), <http://dx.doi.org/10.1029/2010GL046442>.
- Ferronato, M., Castelletto, N., Gambolati, G., 2010. A fully coupled 3-D mixed finite element model of Biot consolidation. *J. Comput. Phys.* 229 (12), 4813–4830. <http://dx.doi.org/10.1016/j.jcp.2010.03.018>.
- Food and Agriculture Organization of the United Nations (FAO), 2022. Water. URL: <http://www.fao.org/water/en/>.
- Fuhrmann, T., Garthwaite, M.C., 2019. Resolving three-dimensional surface motion with InSAR: Constraints from multi-geometry data fusion. *Remote Sens.* 11 (3), 241. <http://dx.doi.org/10.3390/rs11030241>.
- Galloway, D.L., Burbey, T.J., 2011. Review: Regional land subsidence accompanying groundwater extraction. *Hydrogeol. J.* 19 (8), 1459–1486. <http://dx.doi.org/10.1007/s10040-011-0775-5>.
- Galloway, D.L., Hoffmann, J., 2007. The application of satellite differential SAR interferometry-derived ground displacements in hydrogeology. *Hydrogeol. J.* 15 (1), 133–154. <http://dx.doi.org/10.1007/s10040-006-0121-5>.
- Galloway, D.L., Jones, D.R., Ingebritsen, S.E., 1999. Land Subsidence in the United States, vol. 1182, Geological Survey (USGS), <http://dx.doi.org/10.3133/cir1182>.
- Gambolati, G., Teatini, P., 2015. Geomechanics of subsurface water withdrawal and injection. *Water Resour. Res.* 51 (6), 3922–3955. <http://dx.doi.org/10.1002/2014WR016841>.
- George, N., Akpan, A., George, A., Obot, I., 2010. Determination of elastic properties of the overburden materials in parts of Akamkpa, southeastern Nigeria using seismic refraction studies. *Arch. Phys. Res.* 1, 58–71, ISSN: 0976-0970.

- Geuzaine, C., Remacle, J.-F., 2009. Gmsh: A 3-D finite element mesh generator with built-in pre- and post-processing facilities. *Internat. J. Numer. Methods Engrg.* 79 (11), 1309–1331. <http://dx.doi.org/10.1002/nme.2579>.
- Guo, L., Gong, H., Zhu, F., Zhu, L., Zhang, Z., Zhou, C., Gao, M., Sun, Y., 2019a. Analysis of the spatiotemporal variation in land subsidence on the Beijing plain, China. *Remote. Sens.* 11 (10), <http://dx.doi.org/10.3390/rs11101170>.
- Guo, Q., Huang, J., Zhou, Z., Wang, J., 2019b. Experiment and numerical simulation of seawater intrusion under the influences of tidal fluctuation and groundwater exploitation in coastal multilayered aquifers. *Geofluids* <http://dx.doi.org/10.1155/2019/2316271>.
- Guzy, A., Malinowska, A.A., 2020. State of the art and recent advancements in the modelling of land subsidence induced by groundwater withdrawal. *Water* 12 (7), <http://dx.doi.org/10.3390/w12072051>.
- Haagenson, R., Rajaram, H., Allen, J., 2020. A generalized poroelastic model using FEniCS with insights into the Noordbergum effect. *Comput. Geosci.* 135, 104399. <http://dx.doi.org/10.1016/j.cageo.2019.104399>.
- Haghighi, M.H., Motagh, M., 2019. Ground surface response to continuous compaction of aquifer system in Tehran, Iran: Results from a long-term multi-sensor InSAR analysis. *Remote Sens. Environ.* 221, 534–550. <http://dx.doi.org/10.1016/j.rse.2018.11.003>.
- Harbaugh, A.W., 2005. MODFLOW-2005: The U.S. Geological Survey Modular Ground-Water Model—The Ground-Water Flow Process. Report 6-A16, <http://dx.doi.org/10.3133/tm6A16>.
- Harbaugh, A.W., Banta, E.R., Hill, M.C., McDonald, M.G., 2000. MODFLOW-2000, The U.S. Geological Survey Modular Ground-Water Model: User Guide to Modularization Concepts and the Ground-Water Flow Process. Report 00-92, <http://dx.doi.org/10.3133/ofr200092>.
- Heilweil, V., Freethy, G.W., Wilkowske, C., Stolp, B.J., Wilberg, D.E., 2000. Geohydrology and Numerical Simulation of Groundwater Flow in the Central Virgin River Basin of Iron and Washington Counties, Utah. Other Government Series 116, Utah Department of Natural Resources, Division of Water Rights, Salt Lake City, UT, p. 206, URL: <http://pubs.er.usgs.gov/publication/70179116>.
- Heilweil, V.M., Hsieh, P.A., 2006. Determining anisotropic transmissivity using a simplified papadopulos method. *Groundwater* 44 (5), 749–753. <http://dx.doi.org/10.1111/j.1745-6584.2006.00210.x>.
- Helm, D., 1986. COMPAC: a field-tested model to simulate and predict subsidence due to fluid withdrawal. *Austral Geomechan. Comput. Newslett.* 10, 18–20, URL: <http://hdl.handle.net/102.100.100/272626?index=1>.
- Herod, M., 2013. Reading: Porosity and permeability | geology. URL: <https://courses.lumenlearning.com/geo/chapter/reading-porosity-and-permeability/>.
- Herrera-García, G., Ezquerro, P., Tomás, R., Béjar-Pizarro, M., López-Vinielles, J., Rossi, M., Mateos, R.M., Carreón-Freyre, D., Lambert, J., Teatini, P., Cabral-Cano, E., Erkens, G., Galloway, D., Hung, W.-C., Kakar, N., Sneed, M., Tosi, L., Wang, H., Ye, S., 2021. Mapping the global threat of land subsidence. *Science* 371 (6524), 34–36. <http://dx.doi.org/10.1126/science.abb8549>.
- Hesse, M.A., Stadler, G., 2014. Joint inversion in coupled quasi-static poroelasticity. *J. Geophys. Res.: Solid Earth* 119 (2), 1425–1445. <http://dx.doi.org/10.1002/2013JB010272>.
- Hintze, L., 1980. Geologic map of Utah: Utah geological and mineral survey. URL: <https://mrdata.usgs.gov/geology/state/map-us.html>.
- Hoffmann, J., Leake, S.A., Galloway, D.L., Wilson, A.M., 2003. MODFLOW-2000 Ground-Water Model—User Guide to the Subsidence and Aquifer-System Compaction (SUB) Package. Technical Report, (2003–233), U.S. Geological Survey, <http://dx.doi.org/10.3133/ofr03233>.
- Hsieh, P.A., 1996. Deformation-induced changes in hydraulic head during ground-water withdrawal. *Groundwater* 34 (6), 1082–1089. <http://dx.doi.org/10.1111/j.1745-6584.1996.tb02174.x>.
- Hu, X., Bürgmann, R., 2020. Aquifer deformation and active faulting in Salt Lake Valley, Utah, USA. *Earth Planet. Sci. Lett.* 547, 116471. <http://dx.doi.org/10.1016/j.epsl.2020.116471>.
- Hu, X., Lu, Z., Wang, T., 2018. Characterization of hydrogeological properties in Salt Lake Valley, Utah, using InSAR. *J. Geophys. Res.: Earth Surf.* 123 (6), 1257–1271. <http://dx.doi.org/10.1029/2017JF004497>.
- Hurlow, H.A., 1998. The geology of the central Virgin River basin, southwestern Utah, and its relation to ground-water conditions. In: *Water-resources bulletin / Utah Geological Survey*, (26), Utah Geological Survey, Utah Dept. of Natural Resources, Salt Lake City, UT, ISBN: 978-1-55791-614-3.
- Langtangen, H.P., Logg, A., 2016. Solving PDEs in Python. Springer International Publishing, <http://dx.doi.org/10.1007/978-3-319-52462-7>.
- Li, S., Xu, W., Li, Z., 2022. Review of the SBAS InSAR time-series algorithms, applications, and challenges. *Geod. Geodyn.* 13 (2), 114–126. <http://dx.doi.org/10.1016/j.geog.2021.09.007>.
- Loope, D.B., Loope, G.R., Burberry, C.M., Rowe, C.M., Bryant, G.C., 2020. Surficial fractures in the Navajo sandstone, south-western USA: the roles of thermal cycles, rainstorms, granular disintegration, and iterative cracking. *Earth Surf. Process. Landf.* 45 (9), 2063–2077. <http://dx.doi.org/10.1002/esp.4866>.
- Manunta, M., De Luca, C., Zinno, I., Casu, F., Manzo, M., Bonano, M., Fusco, A., Pepe, A., Onorato, G., Berardino, P., De Martino, P., Lanari, R., 2019. The parallel SBAS approach for sentinel-1 interferometric wide swath deformation time-series generation: Algorithm description and products quality assessment. *IEEE Trans. Geosci. Remote Sens.* 57 (9), 6259–6281. <http://dx.doi.org/10.1109/TGRS.2019.2904912>.
- Marston, T.M., Heilweil, V.M., 2012. Numerical Simulation of Groundwater Movement and Managed Aquifer Recharge from Sand Hollow Reservoir, Hurricane Bench Area, Washington County, Utah. USGS Numbered Series 2012-5236, U.S. Geological Survey, Reston, VA, p. 44. <http://dx.doi.org/10.3133/sir20125236>.
- Molina, O., Vilarasa, V., Zeidouni, M., 2017. Geologic carbon storage for shale gas recovery. 13th International Conference on Greenhouse Gas Control Technologies, GHGT-13, 14–18 November 2016, Lausanne, Switzerland, Energy Procedia 13th International Conference on Greenhouse Gas Control Technologies, GHGT-13, 14–18 November 2016, Lausanne, Switzerland, 114, 5748–5760. <http://dx.doi.org/10.1016/j.egypro.2017.03.1713>.
- Osborne, P.S., 1993. Suggested Operating Procedures for Aquifer Pumping Tests. Ground Water Issue (15th in Series). Technical Report, Environmental Protection Agency, Ada, Oklahoma (United States). Robert S. Kerr Environmental Research Laboratory Ada, Oklahoma, URL: <https://www.epa.gov/remedytech>.
- Papadopulos, I.S., 1965. Nonsteady flow to a well in an infinite anisotropic aquifer. In: *Proceedings of the Symposium on Hydrology of Fractured Rocks*. URL: <https://unesdoc.unesco.org/ark:/48223/pf0000141973>.
- Poland, J.F., 1984. Guidebook to Studies of Land Subsidence Due to Ground-Water Withdrawal. URL: <https://unesdoc.unesco.org/ark:/48223/pf0000065167>.
- Qi, Y., Ju, Y., Yu, K., Meng, S., Qiao, P., 2022. The effect of grain size, porosity and mineralogy on the compressive strength of tight sandstones: A case study from the eastern Ordos Basin, China. *J. Pet. Sci. Eng.* 208, 109461. <http://dx.doi.org/10.1016/j.petrol.2021.109461>.
- Salehian Ghamsari, S., Hale, J.S., 2024. Supplementary material for “Can the anisotropic hydraulic conductivity of an aquifer be determined using surface displacement data? A case study”. <http://dx.doi.org/10.5281/zenodo.10890121>.
- Singh, A., 2014. Groundwater resources management through the applications of simulation modeling: A review. *Sci. Total Environ.* 499, 414–423. <http://dx.doi.org/10.1016/j.scitotenv.2014.05.048>.
- Survey, U.G., 2016. National Water Information System data available on the World Wide Web (USGS Water Data for the Nation). URL: <http://waterdata.usgs.gov/nwis/>. (Accessed 31-05-2023).
- Torabi, A., Gabrielsen, R., Fossen, H., Ringrose, P., Skurtveit, E., Andò, E., Marinelli, F., Viggiani, G., Dal Pont, S., Braathen, A., Hovland, A., Bésuelle, P., Alikarami, R., Zalmstra, H., Sokoutis, D., 2015. Strain localization in sandstone and its implications for CO2 storage. *First Break* 33, 81–92. <http://dx.doi.org/10.3997/1365-2397.33.7.81788>.
- Verruijt, A., 1969. Elastic storage of aquifers. In: *Flow Through Porous Media*. Academic Press, New York, NY, USA, pp. 331–376.
- Walker, G., Wang, Q.J., Horne, A.C., Evans, R., Richardson, S., 2020. Estimating groundwater-river connectivity factor for quantifying changes in irrigation return flows in the Murray–Darling Basin. *Australas. J. Water Resour.* 24 (2), 121–138. <http://dx.doi.org/10.1080/13241583.2020.1787702>.
- Zhou, C., Gong, H., Zhang, Y., Warner, T.A., Wang, C., 2018. Spatiotemporal evolution of land subsidence in the Beijing plain 2003–2015 using persistent scatterer interferometry (PSI) with multi-source SAR data. *Remote. Sens.* 10 (4), <http://dx.doi.org/10.3390/rs10040552>.